International Astronautical Congress, Dubai, United Arab Emirates, 25-29 October 2021.

IAC-21-D2-3-2-x66968

Vector Field-based Guidance Development for Launch Vehicle Re-entry via Actuated Parafoil

Stefano Farì[a]*, **Davide Grande**[b]

[a] *German Aerospace Center (DLR), Institute of Space Systems, Department of Guidance, Navigation and Control, Robert-Hooke-Str. 7, 28359, Bremen, Germany,* stefano.fari@dlr.de

[b] *University College London (UCL), Department of Mechanical Engineering, Torrington Place, London, WC1E7JE, United Kingdom,* davide.grande.19@ucl.ac.uk

* Corresponding author

Abstract

In this paper, a launch vehicles re-entry strategy using an actuated parafoil is analyzed. In recent years, this concept is gaining new momentum: it offers a lightweight and cost-effective control solution for autonomous landing of reusable rockets to specific ground or sea coordinates, as well as for mid-air capturing. This landing maneuver requires appropriate modeling together with suitable guidance and control strategies. This work expands upon the following aspects: (1) the development of suitable models for control synthesis and verification; (2) the design of heading control system; (3) the application of a path-following guidance law capable of steering the payload (i.e. the launch vehicle) to the prescribed end-of-mission point. Three models of increasing complexity are proposed based on different assumptions and the dynamics are compared in an ad-hoc simulation environment. MATLAB-Simulink is employed to design two versions of a 6 Degrees Of Freedom (DOF) model accounting for distinct aerodynamic effects. On the other hand, the multi-physics object-oriented language Modelica is used to develop a higher-fidelity 9DOF dynamic model of the system. The latter is then compiled and embedded within MATLAB-Simulink. The same environment allows the implementation of the designed Guidance and Control (G&C) algorithms. The G&C architecture comprises both low-level control loops, regulating course and yaw angles by means of differential steering commands onto the canopy strings, and a guidance layer where the VF path-following is employed. VF methods have already shown remarkable results for fixed-wing unmanned vehicles due to the lower steady-state errors as compared to other approaches, while retaining the potential for realtime implementation. With this work, the method is extended to the application of a launcher recovery. The results of the simulations are investigated, highlighting overall satisfactory performance even in presence of wind disturbances.
Keywords: Launch vehicle re-entry, Parafoil, Vector Field path-following, Modelica, Multi-body modeling

1. Introduction

The rise of commercial companies in the launchers' business has, in the last years, pushed the industry to propose innovative solutions to reduce the operating costs. Reusability of the main boosters or of the subcomponents, proves to be a key factor to reduce the mission costs and in turn to increase access to space. The design of recovery systems hold significant promises to reduce the overall mission costs: in the case of Ariane 6, a recovery system has been found out to cut the costs per launch by 15% [1], whereas the reusability of the SpaceX Falcon 9 boosters is estimated to cut 30% of the launching costs [2].

Recovery strategies to avoid the loss of different stages of the launchers have been investigated since the early space missions, with retro-propulsion, aerodynamic decelerators and landing impact attenuation systems being well-researched options [3]. Mid-Air Recovery strategies involve a main parachute that guarantees the desired deceleration, mounted on the system to be recovered, and in-air randez-vouz with an helicopter that grapples the parachute. The latter carries the descending system to a desired location allowing a safe landing. Landing techniques involving parafoils have been developed over the past 70 years to retrieve unmanned air vehicles or cruise missiles [4]. Despite being limited by the mass of the re-entry system, the option is getting increasingly popular among modern launchers' recovery strategies. In 2020, Rocket Lab carried out several tests to demonstrate the feasibility of recovering the Electron launcher through mid-air helicopter capturing [5, 6]. In a similar fashion, United Launch Alliance is planning

Fig. 1: Rocket Lab mid-air capture concept.

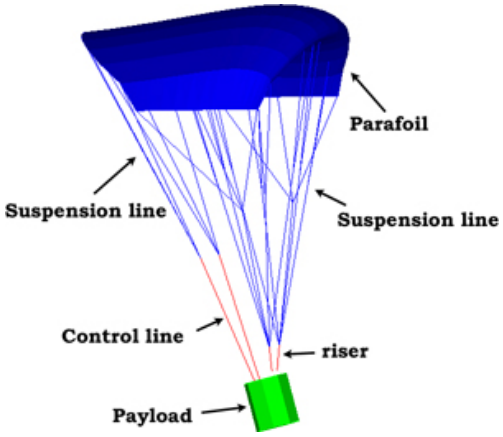

Fig. 2: Simplified parafoil-payload components depiction.

to recover the Vulcan booster main engine with a system comprising a guided parafoil descent and helicopter grasping [7].

Guided parafoils can be employed to recover valuable components of the launchers, approach currently adpoted by SpaceX to retrieve the payload fairings through landing on autonomous boats [8].

Similar recovery systems are gaining popularity in the academia and among student associations due to their low-cost implementation. The increased availability of affordable and reliable off-the-shelf components, together with the growth of compact embedded systems, has in fact led research institutions to start developing proprietary launch systems. For instance, Skyward Experimental Rocketry is employing a recovery system constituted by a Rogallo wing to recover the Rocksanne 2α and Hermes V0 rockets.

To guarantee the safety and accuracy of a landing system including an autonomous parafoil, a robust guidance and control system needs to be designed. The modeling of the system is rendered particularly complex by the highly coupled dynamics linking the parafoil and the oscillating payload. For this purpose, models of increasing complexity are studied and verified in a simulation environment and the guidance system therefore tested. The system under analysis, shown in Figure 2, is composed of a parafoil, a payload and a set of suspension lines. The control is achieved by means of flexible flaps located in the tail section of the wing. Three dynamic models making use of different assumptions are analyzed in this work and are reported in increasing complexity order, as proposed in [9]. The differences in the models are due to assumptions linked to aerodynamic effects, such as the added mass and inertia, and to the choice of the type of joint linking the two bodies.

To simulate the system, MATLAB-Simulink is used in the first instance to verify the dynamics of the simplified models. Following, a Modelica-based approach is deemed the most appropriate given the mutibody nature of the system. Modelica is an open-source object-oriented modeling language that allows multi-domain simulations. It offers a standard Mechanics library allowing to design multibody systems as assembly of rigid-bodies and mechanical interfaces. Modelica has been already proven to deliver state-of-the-art performance when dealing with complex multibody space systems [10–12], or underwater autonomous vehicles [13, 14]. The Modelica model is then exported from Dymola, the IDE of choice, and imported in Simulink through an S-function, to evaluate the performance of the control architecture in a more complex system case.

The proposed G&C system is composed of both low-level course and yaw control loops and a guidance law based on the Vector Field (VF) algorithm [15, 16]. The VF has already been successfully used to control small UAVs [17] but has never been designed to control the landing of a parafoil-payload system.

In this work, different dynamic models are investigated and an approach to design a VF-based guidance strategy is proposed. The paper is organised as follows: in Section 2 different dynamic models are reported, in Section 3 the low-level control architecture design is investigated and in Section 4 the guidance system is detailed. The architecture of the simulator is reported in Section 5. In Section 6 the results obtained are illustrated, while conclusion and future work are reported in Section 7.

2. System modeling

In this section, different dynamic models of a jointed payload-parafoil system are proposed. The system is studied as composed of two different rigid bodies connected by a link representing the suspension lines. In details, three models of increasing complexity are proposed based

on different assumptions. The suggested approach follows the relevant literature on the subject [9, 18]. In the models listed hereby, the main differences lie both in the number of Degrees of Freedom (DOF), and in the nature of the forces and torques acting on either the parafoil or the payload.

6DOF The parafoil and the payload are rigidly connected by means of the suspension lines. This means imposing that the parafoil and the payload have the same attitude. In this model, the apparent mass and inertia are not taken into account.

6DOF+ The parafoil and the payload are rigidly connected by means of the suspension lines, similarly to the 6DOF model. Here, the apparent mass and inertia are taken into account, and the moments generate by the forces displaced with respect to the system center of mass.

9DOF The parafoil and the payload are rigidly connected to a spherical joint. The resulting model dynamics is closer to reality and allows decoupling the attitudes of the parafoil and the one of the payload. The bodies' yaw dynamics are, nevertheless, coupled by means of a spring-damper mechanism, as in [9, 18]. The effect of all forces and torques as in the 6DOF+ model is accounted for.

2.1 Kinematics

Figure 3 shows the adopted reference frames: an inertial-fixed frame $\mathcal{F}_I$, three body-fixed frame (located in the Center of Mass (CM) of the payload $\mathcal{F}_B$, in the CM of the parafoil $\mathcal{F}_P$ and in the one of the overall system $\mathcal{F}_{CM}$) and a wind frame $\mathcal{F}_W$. The inertial frame is selected with a North-East-Down (NED) convention. In what follows the Earth curvature is neglected. The origin of the wind frame coincides with the origin of the body-fixed frame of the parafoil, and has the axes rotated by two aerodynamic angles α_p and β_p, following the standard aerospace convention [19]. Further details about the definition of these angles are reported in Section 2.2.1. In this work, the kinematic quantities related to the parafoil are denoted with the subscript p, whereas the ones linked to the body (also referred to as payload) are reported with the subscript b. Note that in the two 6DOF and 6DOF+ models $\mathcal{F}_B$ and $\mathcal{F}_P$ have the same attitude due to the rigid nature of the joint C.

The reference frame $\mathcal{F}_C$ is oriented as the inertial one $\mathcal{F}_I$. It follows that its position X_c can be expressed as:

$$\dot{X}_c = V_c \tag{1}$$

where V_C represents the C velocity in the $\mathcal{F}_I$ frame.

The vector ξ_p collects the derivative of the Euler Angles of the parafoil, defined as $\xi_p = [\dot{\phi}_p, \dot{\theta}_p, \dot{\psi}_p]^T$ using the

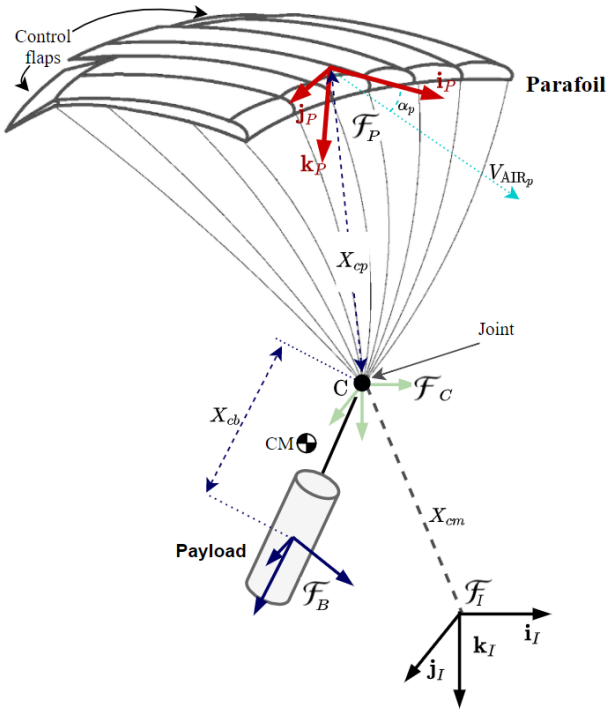

Fig. 3: Reference frames: inertial frame $\{\mathcal{F}_I\}$, parafoil frame $\{\mathcal{F}_P\}$, payload frame $\{\mathcal{F}_B\}$, C frame $\{\mathcal{F}_C\}$. Adapted from [18].

3-2-1 sequence of rotations. In turn, it is related to the angular rates $\omega_p = [p_p, q_p, r_p]^T$ as:

$$\xi_p = \begin{bmatrix} 1 & s_{\phi_p} t_{\theta_p} & c_{\phi_p} t_{\theta_p} \\ 0 & c_{\phi_p} & -s_{\phi_p} \\ 0 & s_{\phi_p}/c_{\theta_p} & c_{\phi_p}/c_{\theta_p} \end{bmatrix} \omega_p \tag{2}$$

where $c_{(\cdot)} = \cos(\cdot)$, $s_{(\cdot)} = \sin(\cdot)$. Similar relations apply to the body ξ_b and respective rates ω_b.

Remark 1. The angular rates of the parafoil and of the payload are equivalent in the 6DOF and 6DOF+ models. As previously explained, ω_p and ω_b do not coincide in the 9DOF model since the attitudes are decoupled due to the spherical joint.

Remark 2. Hereafter, only the 9DOF model is presented for conciseness. Obtaining the 6DOF and 6DOF+ is possible by appropriate modifications of the kinematic and dynamic equations.

It is possible to compute the velocity of the parafoil expressed in $\mathcal{F}_P$ (hence V_p) and of the payload (V_b) in $\mathcal{F}_B$ starting from the velocity of point C:

$$\begin{aligned} V_p &= \mathcal{R}_p(\xi_p)V_C + \omega_p \wedge X_{cp} \\ V_b &= \mathcal{R}_b(\xi_b)V_C + \omega_b \wedge X_{cb} \end{aligned} \tag{3}$$

where X_{cp} and X_{cb} represent the distances from $\mathcal{F}_C$ to $\mathcal{F}_P$ and $\mathcal{F}_B$, respectively. $\mathcal{R}_p$ and $\mathcal{R}_b$ are the 3-2-1 rotation matrices from $\mathcal{F}_I$ to $\mathcal{F}_P$ and $\mathcal{F}_B$ by the Euler angles ξ_p and ξ_b, respectively.

For example:

$$\mathcal{R}_p(\xi_p) = \begin{bmatrix} c_{\theta_p}c_{\psi_p} & c_{\theta_p}s_{\psi_p} & -s_{\theta_p} \\ s_{\phi_p}s_{\theta_p}c_{\psi_p} - c_{\phi_p}s_{\psi_p} & s_{\phi_p}s_{\theta_p}s_{\psi_p} + c_{\phi_p}c_{\psi_p} & s_{\phi_p}c_{\theta_p} \\ c_{\phi_p}s_{\theta_p}c_{\psi_p} + s_{\phi_p}s_{\psi_p} & c_{\phi_p}s_{\theta_p}s_{\psi_p} - s_{\phi_p}c_{\psi_p} & c_{\phi_p}c_{\theta_p} \end{bmatrix}. \tag{4}$$

2.2 Dynamics

In this section, the dynamic effects acting on the system are studied, and the overall dynamic models derived accordingly.

2.2.1 Aerodynamic angles

The aerodynamic coefficients used to model the aerodynamic effects such as drag and lift occurring on the parafoil, are typically modeled as function of the angle of attack α_p and side-slip angle β_p of the parafoil, expressed as:

$$\begin{aligned} V_{\text{AIR}_p} &= \sqrt{u_p^2 + v_p^2 + w_p^2} \\ \alpha_p &= \tan^{-1}\left(\frac{w_p}{u_p}\right) \\ \beta_p &= \sin^{-1}\left(\frac{v_p}{V_{\text{AIR}_p}}\right) \end{aligned} \tag{5}$$

where V_{AIR_p} commonly named as airspeed. The components of the parafoil velocity expressed in frame $\mathcal{F}_P$ are collected in the vector $V_p = [u_p, v_p, w_p]^T$. Similar reasoning holds true for the payload with appropriate substitutions.

2.2.2 Translational dynamics

The translational dynamics equations, written for both the parafoil and payload, can be expressed as:

$$m_p a_p = W^p + F^p + F^{app} + R^p + \Delta F^p \tag{6}$$

$$m_b a_b = W^b + F^b + R^b \tag{7}$$

where:

- m_p and m_b are the masses of the parafoil and the payload, respectively;
- a_p and a_b are the accelerations of parafoil and payload in $\mathcal{F}_P$ and $\mathcal{F}_B$, respectively;
- W^p and W^b are the weight forces of parafoil and payload expressed in the $\mathcal{F}_P$ and $\mathcal{F}_B$ frames, respectively;
- F^p and F^b are the aerodynamic forces of parafoil and payload expressed in the $\mathcal{F}_P$ and $\mathcal{F}_B$ frames, respectively;
- F^{app} is the vector of the apparent forces expressed in the $\mathcal{F}_P$ frame;
- R^p and R^b are the reaction forces exchanged at the joint C and expressed in the $\mathcal{F}_P$ and $\mathcal{F}_B$ frames, respectively;
- ΔF^p the forces generated by the control flaps deflections and expressed in the $\mathcal{F}_P$ frame.

The weight force of the parafoil expressed in frame $\mathcal{F}_P$ can be computed as:

$$W^p = m_p g \begin{bmatrix} -s_{\theta_p} \\ s_{\phi_p}c_{\theta_p} \\ c_{\phi_p}c_{\theta_p} \end{bmatrix} \tag{8}$$

The weight force of the payload expressed in frame $\mathcal{F}_B$ can be computed in the same fashion.

The aerodynamic forces acting on the parafoil can be modeled in the wind frame $\mathcal{F}_W$ as:

$$\bar{F}^p = \frac{1}{2}\rho V_{\text{AIR}_p}^2 S_p \begin{bmatrix} -C_{D,p} \\ 0 \\ -C_{L,p} \end{bmatrix} \tag{9}$$

where S_p is the surface of the parafoil, ρ is the air density and V_{AIR_p} the parafoil airspeed. The characteristic curves of the aerodynamic coefficients expressed with respect to α_p use a quadratic approximation for the drag force, and a linear one for the lift force. These choices are representative of the aerodynamic forces in the majority of the operating conditions [9]. Further care must be taken in case stall conditions need to be investigated. The aerodynamic coefficients of the parafoil can be modeled as:

$$\begin{aligned} C_{D,p} &= C_{D,p_0} + C_{D,p_\alpha}\alpha_p^2 \\ C_{L,p} &= C_{L,p_0} + C_{L,p_\alpha}\alpha_p \end{aligned} \tag{10}$$

In a similar fashion, the aerodynamic forces experienced by the payload can be described as:

$$\bar{F}^b = \frac{1}{2}\rho V_{\text{AIR}_b}^2 S_b \begin{bmatrix} -C_{D,b} \\ 0 \\ 0 \end{bmatrix} \tag{11}$$

where $C_{D,b} = C_{D,b_0} + C_{D,b_\alpha}\alpha_b^2$.
Following, it is possible to rotate the aerodynamic forces

$\bar{F}^p$ and $\bar{F}^b$ from the wind to the parafoil and payload frames as:

$$F^p = \begin{bmatrix} c_{\alpha_p} c_{\beta_p} & -c_{\alpha_p} s_{\beta_p} & -s_{\alpha_p} \\ s_{\beta_p} & c_{\beta_p} & 0 \\ s_{\alpha_p} c_{\beta_p} & -s_{\alpha_p} s_{\beta_p} & c_{\alpha_p} \end{bmatrix} \bar{F}^p$$
$$F^b = \begin{bmatrix} c_{\alpha_b} c_{\beta_b} & -c_{\alpha_b} s_{\beta_b} & -s_{\alpha_b} \\ s_{\beta_b} & c_{\beta_b} & 0 \\ s_{\alpha_b} c_{\beta_b} & -s_{\alpha_b} s_{\beta_b} & c_{\alpha_b} \end{bmatrix} \bar{F}^b \quad (12)$$

The apparent forces account for the effects of the volume of air displaced by the parafoil as a fictitious increase of the mass of the system. This contribution can be expressed as:

$$F^{app} = -M_F a_p - \omega_p \wedge M_F V_p \quad (13)$$

Further details related to the computation of the apparent mass matrix M_F are discussed in Section 2.2.4.

R_p and R_b represent the reaction forces exchanged at the joint, further discussed in [9]. To conclude, the effects of the control force ΔF^p are analyzed in Section 2.3.

2.2.3 Rotational dynamics

The balance of moments for both the parafoil and payload are:

$$I_p \dot{\omega}_p + \Omega_p I_p \omega_p = M^p + M^{app} + M^{R_p} + \Delta M^p \quad (14)$$
$$I_b \dot{\omega}_b + \Omega_b I_b \omega_b = M^{R_b} \quad (15)$$

where:

- I_p and I_b are the inertia matrices of the parafoil and the payload, respectively;
- $\dot{\omega}_p$ and $\dot{\omega}_b$ represent the angular accelerations of $\mathcal{F}_P$ and $\mathcal{F}_B$, respectively;
- Ω_p and Ω_b are the skew-symmetric matrices of ω_p and ω_b, respectively;
- M^p is the vector of the aerodynamic moments expressed in frame $\mathcal{F}_P$;
- M^{app} is the vector of the apparent moments expressed in frame $\mathcal{F}_P$;
- M^{R_p} and M^{R_b} are the moments liked to the reaction forces R_p and R_b and to the twisting resistance at the joint expressed in frame $\mathcal{F}_P$ and $\mathcal{F}_B$, respectively;
- ΔM^p the moments generated by the control flaps deflections and expressed in the $\mathcal{F}_P$ frame.

The aerodynamic moments exerted on the parafoil are defined as:

$$M^p = \frac{1}{2} \rho S_p V_{\text{AIR}_p}^2 \begin{bmatrix} C_l \\ C_m \\ C_n \end{bmatrix} \circ \begin{bmatrix} b \\ c \\ b \end{bmatrix} \quad (16)$$

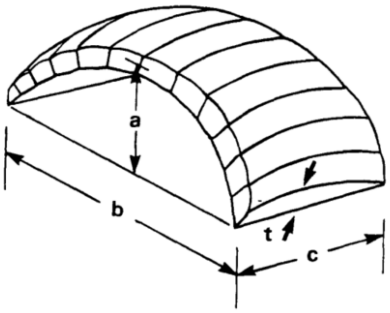

Fig. 4: Parafoil geometry (from [20]).

where $\circ$ is the element wise multiplication, b is the wingspan of the parafoil and c is its main chord, as reported in Figure 4.

It is thus possible to define the aerodynamic coefficients as:

$$C_l = C_{l_\phi} \phi_p + C_{l_p} b \frac{p_p}{2V_{\text{AIR}_p}}$$
$$C_m = C_{m0} + C_{m_\alpha} \alpha_p + C_{m_q} c \frac{q_p}{2V_{\text{AIR}_p}} \quad (17)$$
$$C_r = C_{n_r} b \frac{r_p}{2V_{\text{AIR}_p}}$$

The apparent moments are modeled as:

$$M_{app} = -I_F \dot{\omega}_p - \Omega_p I_F \omega_p - V_p \wedge M_F V_p \quad (18)$$

where I_F represents the apparent inertia tensor, further discussed in Section 2.2.4.

M^{R_p} and M^{R_b} represent the sum of the moments generated by the reaction forces R_p and R_b around point C and of the resistance moments to twisting. The spring-damper system simulating the mechanical damping and stiffness of the suspension line has coefficients k_k and c_c. Further details can be found in Equations (26)-(27) of [18].

To conclude, the effects of the moments ΔM^p generated by the control flaps are analyzed in Section 2.3.

2.2.4 Apparent mass and apparent inertia

A moving body immersed in a fluid induces into motion the surrounding fluid as well. While for standard air vehicles the added mass effects have negligible contributions, for lightly loaded ones, such as parafoils, these terms need to be kept into account. To compute the apparent mass, it is possible to employ the Lissman and Brown formulas [20]:

$$M_F = \begin{bmatrix} A & 0 & 0 \\ 0 & B & 0 \\ 0 & 0 & C \end{bmatrix} \quad (19)$$

where:

$$\begin{array}{cc} k_a = 0.848\pi/4 & A = k_a \rho t^2 b \left(1 + \frac{8}{3}a^3\right) \\ k_b = 0.339\pi/4 & B = k_b \rho [t^2 + 2a^2(1-t^2)]c \\ k_c = \frac{\mathrm{AR}}{1+\mathrm{AR}} \frac{\pi}{4} & C = k_c \rho c^2 b \sqrt{1 + 2a^2(1-t^2)} \end{array} \quad (20)$$

with a the pronounced arch to the canopy shape at the median line, reported in Figure 4, and AR the aspect ratio of the wing defined as $\mathrm{AR} = b/c$.

The inertia tensor can be computed in a similar fashion as:

$$I_F = \begin{bmatrix} I_A & 0 & 0 \\ 0 & I_B & 0 \\ 0 & 0 & I_C \end{bmatrix} \quad (21)$$

where:

$$\begin{array}{cc} k_a^* = 0.055 \frac{\mathrm{AR}}{1+\mathrm{AR}} & I_A = k_a^* \rho c^2 b^3 \\ k_b^* = 0.0308 \frac{\mathrm{AR}}{1+\mathrm{AR}} & I_B = k_b^* \rho c^4 b \left[1 + \frac{\pi}{6}(1+\mathrm{AR})\mathrm{AR}a^2 t^2\right] \\ k_c^* = 0.0555 & I_C = k_c^* \rho t^2 b^3 (1 + 8a^2) \end{array} \quad (22)$$

2.3 The Control surfaces

The control surfaces of the wings are constituted by two flaps, located at the trail of the canopy, and independently actuated one from the other. To steer the system, the flaps need to be deflected asymmetrically, i.e. the flaps angles, namely δ_l (left) and δ_r (right), need to have different values. This generates rolling and yawing moments around the CM of the parafoil that in turn induce the system into rotational motions. To develop the control strategy, the effects of the flaps deflections can be summarized in two quantities, defined as:

$$\begin{aligned} \delta_s &= \min(\delta_l, \delta_r) \\ \delta_a &= \delta_r - \delta_l \end{aligned} \quad (23)$$

where δ_s is the symmetric deflection of the two flaps, that only affect the lateral dynamics by producing a lateral sliding, and δ_a is the difference in the flap deflections. When the two flaps are symmetrically actuated, the drag force on the parafoil increases and the lift decreases. This means that the airspeed and the efficiency of the wing decrease accordingly, having a braking effect on the system.

The deflections of the flaps cause additional forces and moments on the parafoil, reported in Equations (24) and (25), respectively:

$$\Delta F^p = \frac{1}{2}\rho S_p V_{\mathrm{AIR}_p}^2 Q \begin{bmatrix} \delta_a \\ \delta_s \end{bmatrix} \quad (24)$$

where the transformation from wind to parafoil frame has been embedded in Q as:

$$Q = \begin{bmatrix} [C_{L_{\delta_a}} w_p - C_{D_{\delta_a}} u_p]\mathrm{sign}(\delta_a) & C_{L_{\delta_s}} w_p - C_{D_{\delta_s}} u_p \\ -C_{D_{\delta_a}} v_p \mathrm{sign}(\delta_a) & -C_{D_{\delta_s}} v_p \\ [-C_{L_{\delta_a}} u_p - C_{D_{\delta_a}} w_p & -C_{L_{\delta_s}} u_p - C_{D_{\delta_s}} w_p \end{bmatrix}.$$

The control moments are expressed as:

$$\Delta M^p = \frac{1}{2}\rho S_p V_{\mathrm{AIR}_p}^2 \begin{bmatrix} C_{l_{\delta_a}} b/t & 0 \\ 0 & 0 \\ C_{n_{\delta_a}} b/t & 0 \end{bmatrix} \begin{bmatrix} \delta_a \\ \delta_s \end{bmatrix} \quad (25)$$

where t represents the thickness of the parafoil, shown in Figure 4.

2.4 Wind models

To investigate the stability of the system under perturbed conditions and to test the controller performance, wind disturbances have been modeled. Since this study considers only low altitude operating conditions, the Dryden turbulence model and a constant wind are considered. The Dryden model treats the linear and angular velocity components of continuous gusts as spatially varying stochastic processes, and is characterized by rational power spectral densities [21].

3. Low-level control system

As introduced in Section 2.3, imposing a symmetrical deflection is equivalent to initiating a braking maneuver. This control action increases the drag on the wing while decreases its efficiency. On the other hand, an asymmetrical deflection generates rolling and yawing moments that in turn allow the wing to move sideways. Therefore, δ_a is chosen as the control variable for the proposed low-level architecture. Additionally, it is possible to select one of the two flap deflections to be equal to $0°$, so to obtain $\delta_s = 0°$. This means that, for instance, if $\delta_a = 10°$, then $\delta_r = 10°$ and $\delta_l = 0°$.

As it can be seen in Equation (25), δ_a influences both the roll and the yaw angles, in turn allowing both to be used as control variables. Parafoil and payload roll angles (ϕ_p and ϕ_b) may differ significantly during the turning maneuvers due to the spherical joint. On the other hand, due to the damping effect of the joint, payload and parafoil yaw angles tend to converge to the same values (assumption further verified in simulation). Therefore, the yaw angle is chosen for control system design. Additionally, obtaining the measurement of the yaw angle of the parafoil is found to be complex due to inertial sensors usually located in the payload.

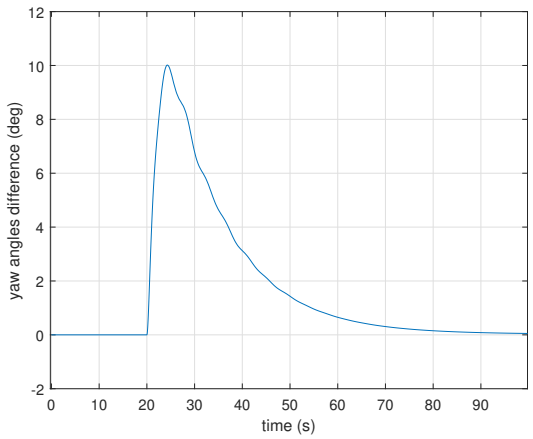

Fig. 5: Yaw angles difference - worst case scenario.

By selecting a maximum value for a step change in the δ_a, chosen to be equal to 20°, it is possible to analyze the effect on the yaw angles ψ_p and ψ_b. The difference between the yaw angle of the parafoil and the one of the payload for a step of 20° in δ_a reference is reported in Figure 5.

It is possible to notice that, even in the worst case scenario, the maximum difference between the ψ_p and ψ_b is bounded below 10°. Is it therefore safe to assume the following relationship between the measured yaw angle (ψ_{meas}) and the yaw angles above mentioned:

$$\psi_{meas} = \psi_b \approx \psi_p \tag{26}$$

Thus, the yaw controller is structured using two nested loops, the inner one designed to track the payload yaw rate $\dot{\psi}_b$ and the outer one for the yaw angle ψ_b. To improve the accuracy of the desired yaw angle tracking, either a sensor needs to be positioned on the parafoil, or an appropriate estimator needs to be designed.

To design the control system, a frequency decoupling approach is chosen. By guaranteeing that the cutting frequency of the closed-loop function is at least one decade faster than the outer one, it is possible to tune the two controllers independently. In particular, the inner loop has a bandwidth of 7 rad/s, whilst the inner of 0.5 rad/s. In Figure 6, the control loops are illustrated: $G_2(s)$ is as integrator $\frac{1}{s}$, while $G_1(s)$ is a first order system, having the transfer function form:

$$G_1(s) = \frac{k}{1 + s\tau} \tag{27}$$

with τ the time constant of the system.

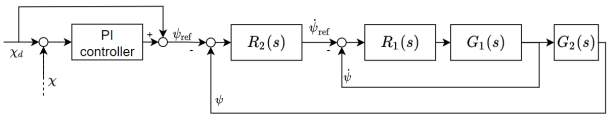

Fig. 6: Overall yaw control scheme approach.

The yaw rate dynamics can be computed based on Equation (2) as:

$$\dot{\psi}_b = r_b + d_{\psi_b} \tag{28}$$

where d_{ψ_b} embeds all the cross coupling terms due to pitch and roll. By deriving Equation (28), it is possible to obtain:

$$\ddot{\psi}_b = \dot{r}_b + \dot{d}_{\psi_b} \tag{29}$$

$$= \frac{1}{2}\rho S_p b \left(C_{n_r} \frac{r_b}{2\bar{V}_{\mathrm{AIR}_b}} + C_{n_{\delta_a}} \delta_a \right) + \dot{d}_{\psi_b} + d_{r_b} \tag{30}$$

where the term d_{r_b} represents the other dynamics discussed previously and $\bar{V}_{\mathrm{AIR}_b}$ the airspeed of the payload at steady state. By considering $\dot{d}_{\psi_p}$ and d_{r_p} as disturbances and assuming $\dot{\psi}_b = r_b$, the yaw dynamics takes the form of Equation (27).

For the design of $R_1(s)$ and $R_2(s)$, a purely proportional law and a full PID with filtered derivative action are selected, respectively. The presence of the integral action in the outer open-loop transfer function ensures that step references can be tracked with zero steady-state error. In addition, the presence of a second integral action in the overall open-loop yaw transfer function ensures that ramp references can be tracked with zero steady-state error as well.

In presence of wind disturbances, however, using the yaw angle as guidance variable may not be sufficient since the system can, despite being correctly oriented, experience lateral drifting while keeping the same heading. For this purpose, the payload course angle χ_b, defined as the angle between $\mathbf{i}_I$ and the ground speed vector $V_{g_b} = V_{\mathrm{AIR}_b} + V_w$ (where V_w represents the wind vector expressed in $\mathcal{F}_B$), is introduced. In other words, the course angle is the sum of the yaw angle, the side-slip angle, and the angle between V_{AIR_b} and V_{g_b}. For this reason, a course-hold loop is added as well. The yaw reference angle is provided as the sum of a feed-forward reference course angle (χ_d) and the output of a PI regulator controlling the course error angle ($\chi_d - \chi_b$), as reported in Figure 6. The feed-forward term is explained by noticing that, when $V_w = 0$ and for small values of β_b, then $\chi_b \approx \psi_b$. The controller gains are tuned in order to minimize course angle response overshoots.

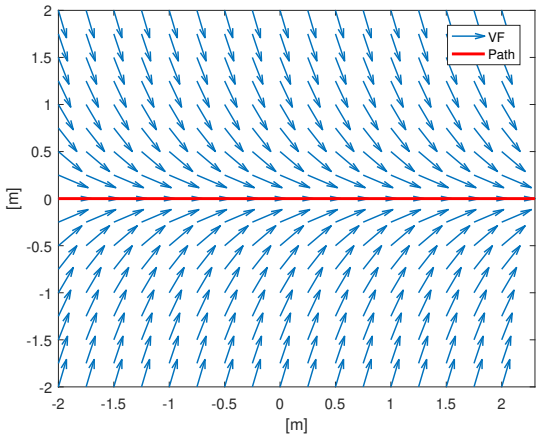

Fig. 7: Vector field straight-line path-following example.

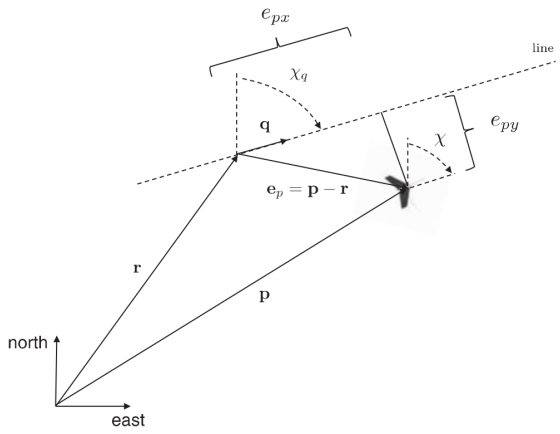

Fig. 8: Straight-line following configuration (adapted from [16]).

4. Vector-field path-following

Once the inner control loops are tuned, the guidance loop can be designed in order to produce a yaw reference angle. Environmental disturbances, due to their unpredictable nature constitute an additional challenge and require robust controls to be developed.

To achieve the goal, a Vector-Field path-following approach can be employed. The reference quantity in the path-following strategies is represented by the spacial deviation from the desired path, namely referred to as cross-track error. Given the desired path, the initial location of the vehicle, and its course angle χ_b, solving the path-following problem means to determine the commanded course angle that minimizes the cross-track error. The segments of path to be tracked in the parafoil-payload application can be developed purely on the horizontal plane, formally the plane $(\mathbf{i}_I, \mathbf{j}_I)$ reported in Figure 3. The VF algorithm is in fact based on the assumption that the vehicle has a low flight path angle $\gamma_p = \theta_p - \alpha_p$. This allows writing a simplified model for guidance as:

$$\dot{X}_b(1) = V_{g_b} \cos \chi_b \tag{31}$$

$$\dot{X}_b(2) = V_{g_b} \sin \chi_b \tag{32}$$

where $\dot{X}_b$ is the velocity of the payload in inertial coordinates. In Figure 7 an example of the desired headings generated by a VF-algorithm for the case of a straight-line tracking is reported. The assumptions made so far, are summarized hereby:

1. the yaw angle of the payload is measurable ($\psi_{meas} = \psi_b$);
2. the difference of the yaw angle of the payload and the one of the payload is bounded ($\psi_b \approx \psi_p$);
3. the airspeed is constant or slowly varying;
4. the course angle of the payload χ_b is measurable;
5. the flight path angle γ_p is relatively small.

To drive the vehicle to a desired landing location, two path primitives need to be tracked: a line and an orbit. These two can be combined upon need and used to reach the landing point.

4.0.1 Straight-line following

A straight-line can be described with a quantity $\mathbf{r}$, hence the origin of the path, and $\mathbf{q}$, a unit inertial vector that indicates the desired direction of travel. The course angle of the line is:

$$\chi_q = \text{atan2}\left(\frac{\mathbf{q}(2)}{\mathbf{q}(1)}\right) \tag{33}$$

The path-following implementation can be simplified by changing the reference from the inertial frame to the line path one. It is possible to define:

$$R_i^p = \begin{bmatrix} \cos \chi_q & \sin \chi_q \\ -\sin \chi_q & \cos \chi_q \end{bmatrix} \tag{34}$$

The cross-track error vector can be defined as:

$$\mathbf{e}_p = \begin{bmatrix} e_{px} \\ e_{py} \end{bmatrix} = R_i^p (\mathbf{p} - \mathbf{r}) \tag{35}$$

where $\mathbf{p}$ is the position of the system in the inertial frame. The quantities can be appreciated in Figure 8.

The objective is to design the vector field so that when e_{py} is large the system is directed to approach the path

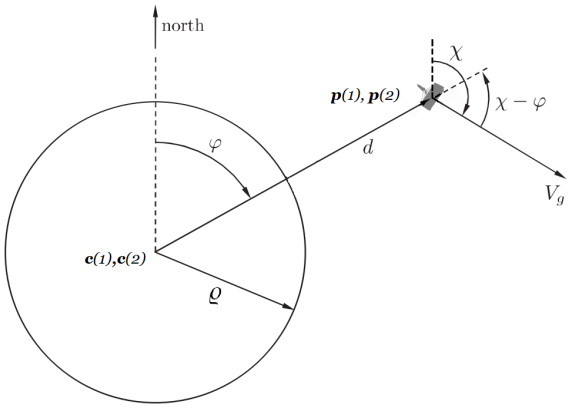

Fig. 9: Orbit following configuration (adapted from [15]).

with course $\chi_\infty \in [0, \frac{\pi}{2})$, and so that as e_{py} approaches zero, the desired course approaches zero too. We define the desired course as:

$$\chi_d(e_{py}) = \chi_q - \chi_\infty \frac{2}{\pi} \tan^{-1}(k_{line} e_{py}) \tag{36}$$

where k_{line} is a positive constant that influences the rate of transition from χ_∞ to zero. Large values of k_{line} cause abrupt transitions, while small values cause longer and smoother transitions in the desired course. Clearly, $-\frac{\pi}{2} < \chi_d(e_{py}) < \frac{\pi}{2}$. In [15] formal proof of stability of Equation (36) is given.

One note should be done regarding χ_q: the given formula makes the system not turning coherently with the shortest path. As an example, if the angle is slightly less than $+\pi$ and the course is zero, the system turns right to align with the path. As a counterexample, if χ_q is slightly less than $-\pi$ the system will turn left instead of right. To address the issue, it is possible to define χ_q as:

$$\chi_q = \text{atan2}(\mathbf{q}(2), \mathbf{p}(1)) + 2\pi m \tag{37}$$

where m is a constant such as $\chi_q - \chi \in [-\pi; +\pi]$.

4.0.2 Orbit following

Similarly to the line, it is possible to define $\lambda = \pm 1$ to denote a clockwise or counter-clockwise orbit, $\mathbf{c}$ to represent the coordinates of the center of the orbit, and ϱ the orbit radius. In Figure 9 the definition of φ (phase angle of relative position) can be seen.

Here, a course field for the orbit path is given by:

$$\chi_d(\varphi) = \varphi + \lambda \left[\frac{\pi}{2} + \tan^{-1}\left(k_{orbit} \left(\frac{\tilde{d}}{\varrho} \right) \right) \right]. \tag{38}$$

Note that k_{orbit} is a positive tuning parameter that specifies the rate of transition from $\lambda\pi/2$ to zero, and d is always positive being the distance to the orbit center. The cross-track error is here evidenced as $\tilde{d} = d - \varrho$. Further details about this control law can be found in [16] and [15]. Also here, φ should be computed as follows to avoid the aforementioned problem:

$$\varphi = \text{atan2}(\mathbf{p}(2) - \mathbf{c}(2), \mathbf{p}(1) - \mathbf{c}(1)) + 2\pi m. \tag{39}$$

4.1 Path manager

In order to steer the payload towards the desired landing location it is possible to combine a straight-line segment, leading from the starting point an area above the landing point, with a final orbit. Therefore, it is possible to implement a path manager that switches from the straight-line path-following to the orbit path-following law when the parachute is sufficiently close the the orbit. It is therefore possible to define d_{boundary} as:

$$d_{\text{boundary}} \in \left(\frac{3}{2}\varrho, 2\varrho \right).$$

When the distance of the system from the landing point is less than d_{boundary}, the path manager hot-switches to the loiter control law.

To steer the system towards the orbit center, it is possible to start noticing that the descent rate is constant. Therefore, the estimated time before landing is approximately $t_{\text{land}} \simeq h/\dot{h}$, where h is the current altitude. Moreover, as a first approximation, it is possible to compute the time required to the system to converge to the center as:

$$\begin{aligned} d_{\text{final}} &= \sqrt{h^2 + \varrho^2} \\ t_{\text{toCenter}} &= d_{\text{final}} / \sqrt{\dot{h}^2 + V_{\text{AIR}_p}^2} \end{aligned} \tag{40}$$

When $t_{\text{land}} < t_{\text{toCenter}}$, the orbit radius ϱ is reduced to a very small value; this avoids the necessity of compute a new straight-line reference for moving from the current position to the center.

5. Simulator architecture

The plant models described in Section 2, as well as the G&C algorithms, are implemented in the MATLAB-Simulink environment (Figure 10). This includes a plant subsystem containing three different variants, one per each model (6DOF, 6DOF+, and 9DOF). The other subsystem represent the guidance, control and the environmental disturbances, and do not require further explanation.

The Modelica model has been implemented in the Dymola IDE, as in Figure 11. To this purpose, the Multibody

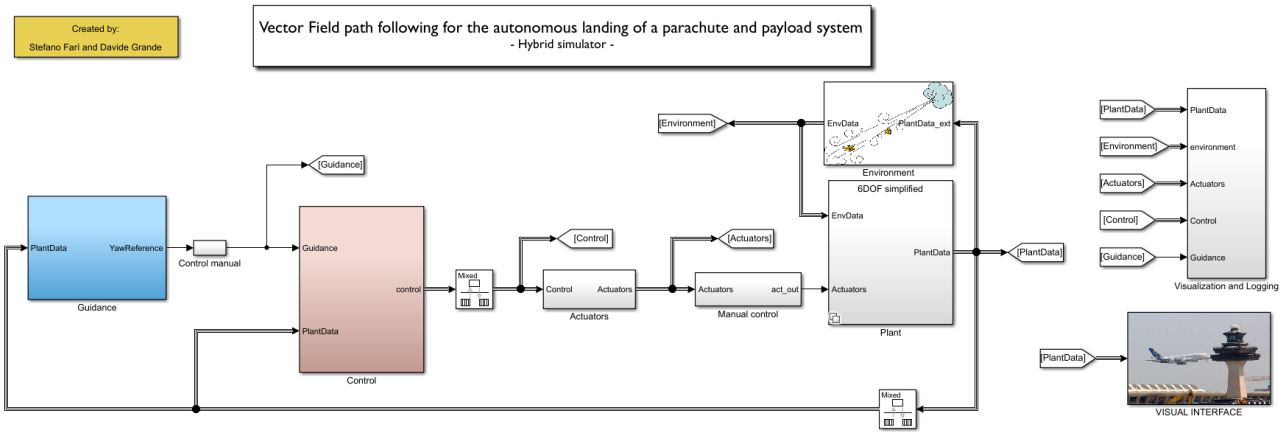

Fig. 10: Simulink base subsystem diagram view.

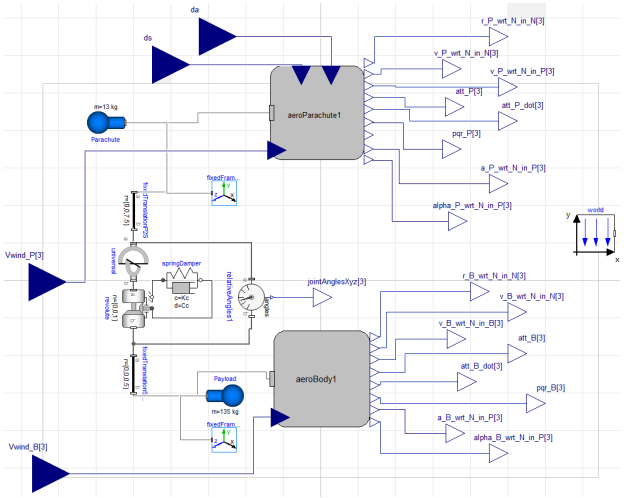

Fig. 11: Parafoil-payload system superclass implemented in Dymola.

Param.	Value	Param.	Value
m_p	13	m_b	135
a	1	b	7
c	3	t	3
S_b	0.500	S_p	21
$\|X_{cb}\|$	0.500	$\|X_{cp}\|$	7.500
I_b	diag(5.620)	$I_p(1,1)$	53.180
$I_p(2,2)$	9.840	$I_p(3,3)$	62.830
C_{L,p_0}	0.400	C_{L,p_α}	2
C_{D,p_0}	0.150	C_{D,p_α}	1
C_{D,b_0}	0.150	C_{D,b_α}	1
C_{l_p}	-0.100	C_{l_ϕ}	-0.050
C_{m_q}	-2	C_{m_0}	0.018
C_{n_r}	-0.070	C_{m_α}	-0.200
$C_{L_{\delta_a}}$	1e-4	$C_{L_{\delta_s}}$	0.210
$C_{D_{\delta_a}}$	1e-4	$C_{D_{\delta_s}}$	0.300
$C_{l_{\delta_a}}$	21e-4	$C_{n_{\delta_a}}$	0.004
k_k	0.350	c_c	4.700

Table 1: Model parameters (reported in SI units).

package of the Modelica Standard Library (MSL) [22] has been employed: the latter can be seen via the usage of the `Body` class for modeling the parafoil and the payload, and the connecting elements among them. All the forces and torques related to either one or the other, are enclosed in the `AeroParachute` and `AeroBody` classes, including forces and torques described in Section 2. In this model, the inertial-referenced wind vector is an input of the whole model, which is then compiled as S-function and embedded in the Simulink simulator.

6. Simulation results

In this section, the guidance and control system is verified and results obtained are discussed. All the parameters used for the models are reported in Table 6. In all simulations, the parafoil-payload system is set to start with an initial position with respect to $\mathcal{F}_I$ of $[0, 0, -1000]$ m and velocity of $[6, 0, 0.1]$ m/s. The initial Euler angles are set to zero, as well as their respective angular velocities. In the following figures, only the positions of the parafoil are shown for simplicity.

In Figure 12, the response to a commanded step in yaw

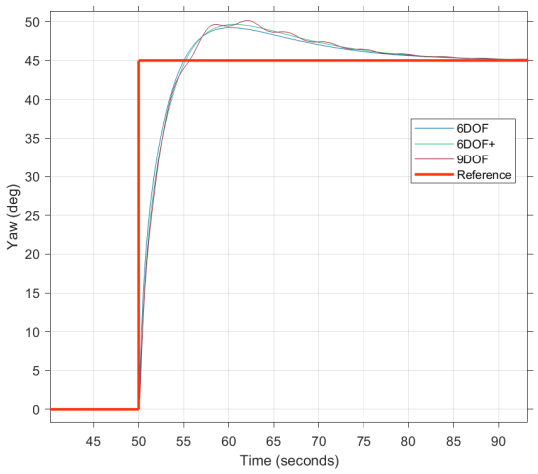

Fig. 12: Comparison of the three models response to a yaw step input.

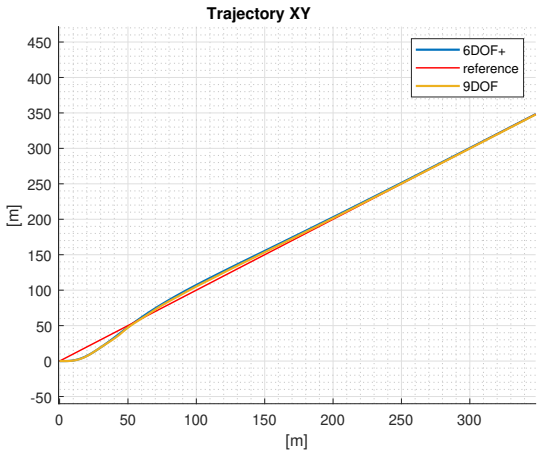

Fig. 13: Vehicle trajectory in the $(\mathbf{i}_I - \mathbf{j}_I)$ plane for a straight-line path maneuver.

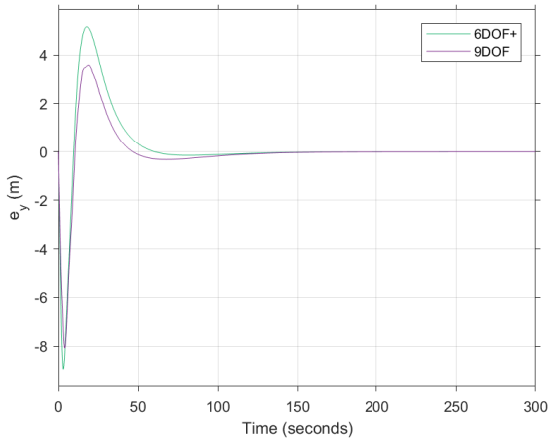

Fig. 14: Cross-track error for a straight-line path maneuver.

is shown, to highlight the performance of the three models: it is noticeable how the dynamics of the 6DOF and 6DOF+ are comparable, with the 9DOF exhibiting low amplitude oscillations due to the swinging payload. Given that the differences found between the 6DOF and 6DOF+ models are found to be negligible, hereafter, only the 6DOF+ is used for comparison with the 9DOF.

Figures 13 and 14 show the performance of the straight-line path-following guidance on both models. In particular, Figure 13 reports the view from the $(\mathbf{i}_I - \mathbf{j}_I)$ plane of the vehicle trajectory, whereas the Figure 14 shows the cross-track error, which asymptotically reaches zero as desired. The VF has been tuned so to achieve the least oscillations in both cases, with a $\chi_\infty = 80°$ and $k_{line} = 0.01$.

In Figures 15 and 16 the trajectory and the cross-track error $\tilde{d}$ for an orbiting maneuver are reported, respectively. Also in this case scenario, the cross-track error is found to reach zero steady-state values by selecting $k_{orbit} = 1$.

Similarly, Figures 17 and 18 report trajectory and cross-track error for a path composed of both a straight-line and of an orbit. Despite the abrupt change in the reference course angle generated in transition instant (Time = 75 s), the VF is eventually capable of achieve zero steady-state error.

Lastly, the 9DOF model is simulated in presence of wind disturbances. Both constant wind vector with magnitude of 2 m/s and a fixed angle with respect to $\mathbf{i}_I$ of $\kappa = 90°$ is applied, as well as a Dryden turbulence model described in Section 2.4. Furthermore, the path manager is set up so to steer the system towards the center of the orbit before touchdown. Figures 19 and 20 show the parafoil-payload system trajectory in the horizontal and vertical planes, respectively. Note that in Figure 20, the sign of the altitude is flipped with respect to the NED convention previously introduced. It is shown that even in presence of disturbances, does not generate unstable dynamics during the descent and landing. Nevertheless, more extensive simulation campaigns are to be performed under more realistic environmental conditions.

7. Conclusion and future work

In this work, the Vector Field path-following strategy has been applied for the first time to the case of parafoil-

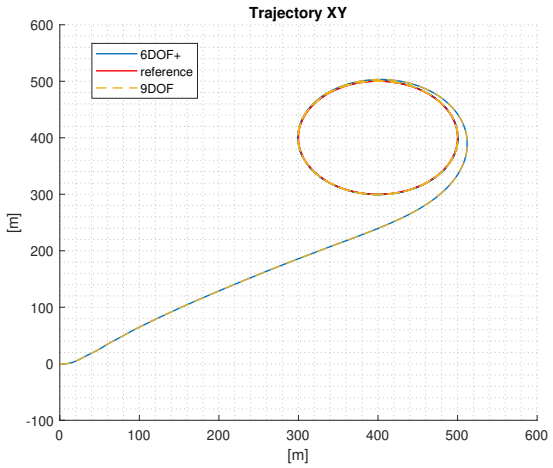

Fig. 15: Vehicle trajectory in the $(\mathbf{i}_I - \mathbf{j}_I)$ plane for an orbit maneuver.

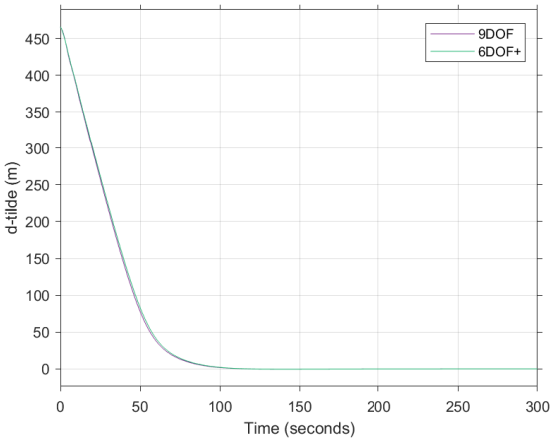

Fig. 16: Cross track error for an orbit maneuver.

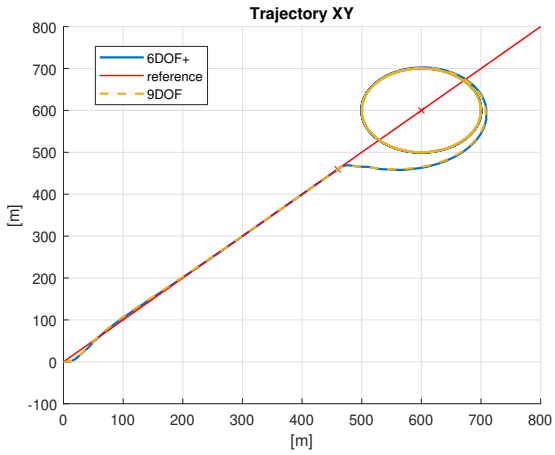

Fig. 17: Vehicle trajectory in the $(\mathbf{i}_I - \mathbf{j}_I)$ plane for a combined maneuver (straight-line and orbit).

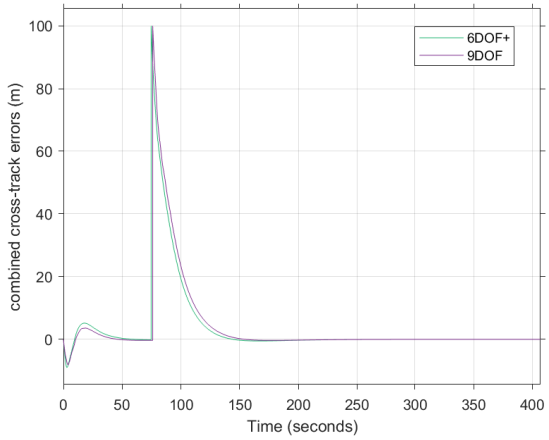

Fig. 18: Cross track error for a combined maneuver (straight-line and orbit).

payload systems. This is specifically significant, since the ability of such an algorithm to autonomously drive towards a landing point can be exploited by atmospheric re-entry vehicles and increase system safety and cost-effectiveness. To achieve this goal, three different models have been developed and implemented in a simulation environment. A 9DOF model has been developed using Modelica language, better suited than causal simulation environments (e.g. Simulink) for multibody systems representations. The capability to switch with ease between models of different complexity, makes it also easier to evaluate the performance of G&C system and its robustness to different mechanical and aerodynamic assumptions.

An easy-to-design control system for course angle tracking has been proposed. The selected approach keeps into account the limitation on the quantities that can be potentially measured onboard. Where needed, simplifying assumptions are highlighted and further verified in simulation.

The proposed implementation of the Vector Field path-following laws shows that this G&C strategy is a valid candidate for further studies and in-field tests. The straight-line and orbit primitives can be accurately tracked both in absence and presence of wind disturbances. These preliminary results are independent of the selected model for verification.

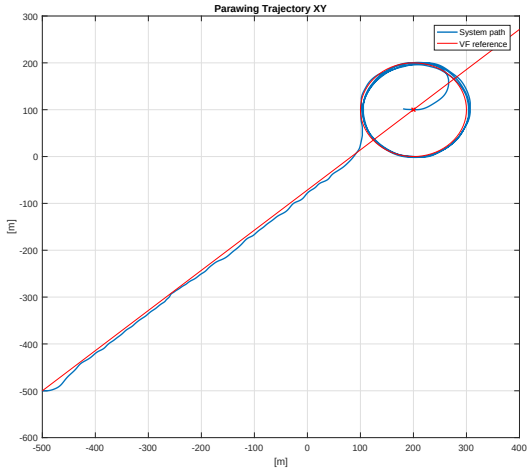

Fig. 19: Total path tracking with wind disturbances ($(\mathbf{i}_I, \mathbf{j}_I)$ plane).

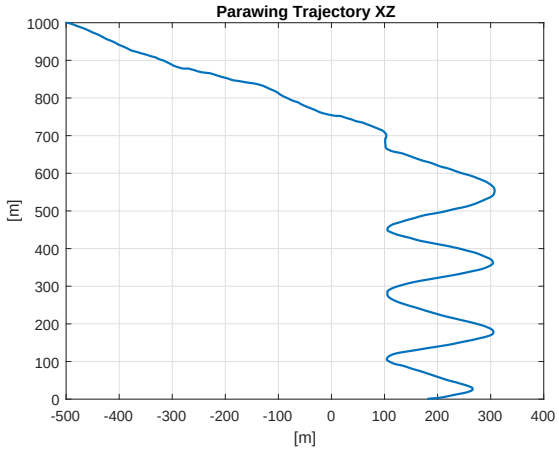

Fig. 20: Total path tracking with wind disturbances ($(\mathbf{i}_I, \mathbf{k}_I)$ plane).

Despite these achievements, several improvements are considered for future developments:

1. the models can be further refined and should include a payload resembling an actual launch vehicle, with consequent changes in the whole system dynamics;
2. the parafoil model can include the deployment shock effect at the beginning of the controlled descent;
3. wind models can be extended to include gusts;
4. actuation strings dynamics can be included in the model and in the control system synthesis process;
5. the simulations can include an extended flight envelope at higher altitudes;
6. Monte-Carlo campaigns can be conduced to examine the method validity also in presence of model uncertainties;
7. the feasibility of a mid-air capture while following a line and under atmospheric disturbances, can be investigated;
8. the control variable δ_s can be exploited to achieve a better stability or for the inclusion of more precise braking maneuvers at terminal landing.

References

[1] C. Dek, J.-L. Overkamp, A. Toeter, T. Hoppenbrouwer, J. Slimmens, J. van Zijl, P. A. Rossi, R. Machado, S. Hereijgers, V. Kilic *et al.*, "A recovery system for the key components of the first stage of a heavy launch vehicle," *Aerospace Science and Technology*, vol. 100, p. 105778, 2020.

[2] L. A. Davis, "First stage recovery," *Engineering*, vol. 2, no. 2, pp. 152–153, 2016.

[3] M. Ragab and F. M. Cheatwood, "Launch vehicle recovery and reuse," in *AIAA Space 2015 Conference and Exposition*, 2015, p. 4490.

[4] M. Gravlee, B. Kutter, F. Zegler, B. Mosley, and R. Haggard, "Partial rocket reuse using mid-air recovery," in *AIAA SPACE 2008 Conference & Exposition*, 2008, p. 7874.

[5] "Rocket Lab to Recover Electron Booster on Next Mission," https://www.rocketlabusa.com/about-us/updates/rocket-lab-to-recover-electron-booster-on-next-mission/.

[6] M. Darley and P. Beck, "Return to sender: Lessons learned from rocket lab's first recovery mission," in *Small Satellite Conference*, 2021.

[7] J. DiNonno, F. Cheatwood, S. Hughes, M. Ragab, R. Dillman, R. Bodkin, C. Zumwalt, and R. Johnson, "Hiad on ula (hula) orbital reentry flight experiment concept," in *NASA*, 2016.

[8] D. Bonetti, G. Medici, G. B. Arnao, S. Salvi, A. Fabrizi, and M. Kerr, "Reusable payload fairings: Mission engineering and gnc challenges," in *8TH European Conference for Aeronautics and Space Sciences (EUCASS)*, 2019.

[9] C. Toglia and M. Vendittelli, "Modeling and motion analysis of autonomous paragliders," Università di Roma "La Sapienza", Tech. Rep. Report nr.5, 2010.

[10] S. Farì, D. Seelbinder, and S. Theil, "Advancing Modeling and Simulation of Vertical Landing Vehicles with Fuel Slosh Dynamics," *Paper submitted for publication*, 2021.

[11] P. Acquatella and M. J. Reiner, "Modelica stage separation dynamics modeling for End-to-End launch vehicle trajectory simulations," in *Proceedings of the 10th International Modelica Conference - Lund, Sweden - Mar 10-12, 2014*, H. Tummescheit and K.-E. Årzén, Eds., vol. 96. Lund, Sweden: LiU Electronic Press, Mar. 2014, pp. 589–598.

[12] L. E. Briese, P. Acquatella B, and K. Schnepper, "Multidisciplinary modeling and simulation framework for launch vehicle system dynamics and control," *Acta Astronautica*, vol. 170, pp. 652–664, May 2020.

[13] D. Grande, L. Bascetta, and A. Martins, "Modeling and simulation of a spherical vehicle for underwater surveillance," in *OCEANS 2018 MTS/IEEE Charleston*. IEEE, 2018, pp. 1–7.

[14] D. Grande, L. Huang, C. Harris, P. Wu, G. Thomas, and E. Anderlini, "Open-source simulation of underwater gliders," in *OCEANS 2021 Porto / San Diego*. IEEE, 2021.

[15] R. W. Beard and T. W. McLain, *Small Unmanned Aircraft: Theory and Practice*. Princeton, N.J: Princeton University Press, 2012.

[16] D. Nelson, D. Barber, T. McLain, and R. Beard, "Vector Field Path Following for Miniature Air Vehicles," *IEEE Transactions on Robotics*, vol. 23, no. 3, pp. 519–529, Jun. 2007.

[17] S. Farì, X. Wang, S. Roy, and S. Baldi, "Addressing Unmodeled Path-Following Dynamics via Adaptive Vector Field: A UAV Test Case," *IEEE Transactions on Aerospace and Electronic Systems*, vol. 56, no. 2, pp. 1613–1622, Apr. 2020.

[18] N. Slegers and M. Costello, "Aspects of Control for a Parafoil and Payload System," *Journal of Guidance, Control, and Dynamics*, vol. 26, no. 6, pp. 898–905, Nov. 2003.

[19] B. L. Stevens, *Aircraft Control and Simulation*. John Wiley and Sons, 2016.

[20] P. Lissaman and G. Brown, "Apparent mass effects on parafoil dynamics," in *Aerospace Design Conference*. Irvine,CA,U.S.A.: American Institute of Aeronautics and Astronautics, Feb. 1993.

[21] T. M. I. Hakim and O. Arifianto, "Implementation of dryden continuous turbulence model into simulink for lsa-02 flight test simulation," in *Journal of Physics: Conference Series*, vol. 1005, no. 1. IOP Publishing, 2018, p. 012017.

[22] "Modelica Standard Library," Modelica Association, Jan. 2021. [Online]. Available: https://github.com/modelica/ModelicaStandardLibrary